Phosphorized $CoNi_2S_4$ Yolk-Shell Spheres for Highly Efficient Hydrogen Production via Water and Urea Electrolysis

Xue Feng Lu, Song Lin Zhang, Wei Lok Sim, Shuyan Gao, and Xiong Wen (David) Lou**

[*] Prof. S. Y. Gao
School of Materials Science and Engineering, Henan Normal University, Xinxiang, Henan 453007, P.R. China. Email: shuyangao@htu.cn

Dr. X. F. Lu, S. L. Zhang, W. L. Sim, Prof. X. W. Lou
School of Chemical and Biomedical Engineering, Nanyang Technological University, 62 Nanyang Drive, Singapore, 637459, Singapore
Email: xwlou@ntu.edu.sg; davidlou88@gmail.com Webpage: https://personal.ntu.edu.sg/xwlou/

Abstract

Exploring earth-abundant electrocatalysts with excellent activity, robust stability, and multiple functions is crucial for electrolytic hydrogen generation. Herein, porous phosphorized $CoNi_2S_4$ yolk-shell spheres (P-$CoNi_2S_4$ YSSs) are rationally designed and synthesized by a combined hydrothermal sulfidation and gas-phase phosphorization strategy. Benefiting from the strengthened Ni^{3+}/Ni^{2+} couple, enhanced electric conductivity, and hollow structure, the P-$CoNi_2S_4$ YSSs exhibit excellent activity and durability towards hydrogen/oxygen evolution and urea oxidation reactions in alkaline solution, affording low potentials of -0.135 V, 1.512 V, and 1.306 V (versus reversible hydrogen electrode) at 10 mA cm^{-2}, respectively. Remarkably, when used as the anode and cathode simultaneously, the P-$CoNi_2S_4$ catalyst merely requires a cell voltage of 1.544 V in water splitting and 1.402 V in urea electrolysis to attain 10 mA cm^{-2} with excellent durability for 100 h, outperforming most of the reported nickel-based sulfides and even noble-metal-based electrocatalysts. This work therefore not only promotes the application of sulfides in electrochemical hydrogen production but also provides a feasible approach for urea-rich wastewater treatment.

Keywords: $CoNi_2S_4$, phosphorization, hydrogen, urea, electrolysis

Renewable energy-driven electrolytic hydrogen generation has been recognized as an eco-friendly manner to alleviate the energy crisis and environmental issues faced by the international community.[1-3] However, the unfavorable thermodynamics and sluggish kinetics of both cathodic reduction and anodic oxidation reactions severely restrict the hydrogen production rate and energy efficiency.[3-7] Noble-metal-based electrocatalysts are known as the most active catalysts for electrolytic hydrogen production, but their large-scale application is largely hindered by the prohibitive costs, low reserves, and unsatisfactory stability.[8-10] Recent years have witnessed the rapid development of earth-abundant electrocatalysts, especially towards hydrogen/oxygen evolution reactions (HER/OER) for alkaline water splitting.[11,12] But most of them do not possess excellent performance for both HER and OER in the same electrolyte due to their incompatible activity over different pH ranges.[10] In addition, the high thermodynamic equilibrium potential (1.23 V versus reversible hydrogen electrode (vs. RHE)) of OER undoubtedly increases the energy consumption of hydrogen production.[7,9] Therefore, to reduce the overall cell voltage and manufacturing cost, exploring more efficient low-cost multifunctional electrocatalysts and hybrid water electrolysis systems coupled with some diligent anodic oxidations is highly desired.

Urea oxidation reaction (UOR) has been reported as an ideal alternative to OER due to its much lower thermodynamic equilibrium potential (0.37 V vs. RHE), enabling the urea electrolysis a promising electrochemical approach for energy-saving and high-efficiency hydrogen production.[13-16] Moreover, urea-rich wastewater is generated from industrial synthesis and sanitary sewage, thus making urea electrolysis attractive for mitigating the problem of urea-rich water pollution.[15] However, the complicated six-electron transfer process of UOR ($CO(NH_2)_2 + 6OH^- \rightarrow N_2 + 5H_2O + CO_2 + 6e^-$) leads to sluggish kinetics and higher practical cell voltage of urea electrolysis.[16] Among all the transition metal-based electrocatalysts, nickel (Ni) is the most widely used element for energy and environmental applications.[17] For example, Raney Ni and Ni alloys have been widely used in conventional alkaline water electrolyzers due to their low cost and high efficiency.[18] Recently, Ni

and Ni-based compounds have received great attention for the UOR to accelerate the kinetics, during which they undergo an oxidation process to generate active Ni^{3+} (NiOOH) for catalyzing UOR.[13,15,19] Nevertheless, there are few reports on trifunctional Ni-based electrocatalysts for highly efficient hydrogen production via both water and urea electrolysis.

Among all the Ni-based electrocatalysts, sulfides have shown promising trifunctional electrocatalytic performance towards HER, OER, and UOR, and various strategies have been applied to improve their performance. One appealing idea is composition manipulation by heteroatom doping or substitution, which can modulate the adsorption energies of intermediates by optimizing the electronic structure of catalysts. For example, Yin et al. prepared different metal-doped NiS_2 (M-NiS_2, M= Fe, Co, Cu) nanosheets, in which Co-NiS_2 achieved prominent HER performance in alkaline media due to the optimal e_g^1 electron configuration.[20] Besides, cation doping can also significantly increase the content of high-valence Ni^{3+} (NiOOH) species, which have been identified as the catalytic active sites for anodic OER and UOR.[14,19,21,22] Recently, phosphorization has also been widely reported to improve the HER intrinsic activity and conductivity by tuning the electronic structure and distorting the lattices of the parent sulfides.[23-26] Morphological and structural engineering is another efficient approach for enhancing the catalytic performance through exposing more active sites. In particular, porous yolk-shell structures are favored because of their high specific surface area, large void volume, and reduced ion-diffusion path.[27-29]

Inspired by these advancements in multi-element Ni-based sulfide electrocatalysts, we rationally design and synthesize porous phosphorus substituted $CoNi_2S_4$ yolk-shell spheres (P-$CoNi_2S_4$ YSSs) via a facial hydrothermal sulfidation and subsequent gas-phase phosphorization strategy (**Figure 1**). Benefiting from the advantageous features of bimetallic elements, high electronic conductivity and enriched Ni^{3+} content induced by phosphorization, as well as unique hollow structure, the obtained P-$CoNi_2S_4$ YSSs electrocatalyst exhibits superior activity and stability towards HER, OER, and UOR

in alkaline media, yielding low potentials of -0.135 V, 1.512 V, and 1.306 V vs. RHE at 10 mA cm^{-2}, respectively. Consequently, the P-$CoNi_2S_4$||P-$CoNi_2S_4$ catalyst couple for water electrolysis only needs a low cell voltage of 1.544 V to steadily drive a benchmark current density of 10 mA cm^{-2} for 100 h, much better than that of commercial Pt/C||RuO_2 couple. Remarkably, the cell voltage can be further reduced to 1.402 V when 0.5 M urea is added, almost rivaling the state-of-the-art urea electrolysis. This work highlights the effectiveness of Ni-based bimetallic sulfides for water and urea electrolysis and strengthens the significance of the nickel valence for performance improvement, hence enabling cost-effective and energy-saving electrochemical hydrogen production.

Uniform CoNi-glycerate solid spheres (CoNi-G SSs) are prepared by a previously reported method with slight modification (see the experimental details in Supporting Information (SI)).[28] Field-emission scanning electrode microscopy (FESEM) and transmission electron microscopy (TEM) images demonstrate the smooth surface and solid nature of CoNi-G SSs with an average diameter of 490 nm (**Figure 2**a,d; Figure S1a,b, SI). X-ray diffraction (XRD) pattern (Figure S1c) and energy-dispersive X-ray (EDX) spectrum (Figure S1d) indicate the amorphous phase of metal alkoxides and the chemical composition of a Co/Ni atomic ratio around 1/2, respectively.[30] $CoNi_2S_4$ YSSs are obtained via the chemical etching/anion exchange reactions between CoNi-G SSs and thioacetamide solution under hydrothermal conditions (see the experimental details in SI). FESEM and TEM images show the rough surface and void space between the interior solid core and the outer porous shell of $CoNi_2S_4$ YSSs with an average diameter of 570 nm (Figure 2b,e; Figure S2a, SI). Subsequently, P-$CoNi_2S_4$ YSSs are achieved by a gas-phase phosphorization of $CoNi_2S_4$ YSSs (see the experimental details in SI). The porous yolk-shell structure is well preserved with a slightly reduced diameter of 520 nm (Figure 1c,f; Figure S2b). A typical TEM image of an individual P-$CoNi_2S_4$ YSS further demonstrates that the yolk-shell structure with a porous thin shell (about 35 nm in thickness) is assembled by ultrafine nanoparticles (Figure 2g), which is beneficial for the exposure of active sites. The high-resolution TEM (HRTEM) and inverse fast Fourier transform (IFFT) images

(Figure 2h) clearly show two sets of distinct lattice fringes with interplanar spacings of 0.24 and 0.28 nm, which are readily assigned to the (400) and (311) planes of $CoNi_2S_4$ (JCPDS card No. 24-0334), respectively. The high-angle annular dark-field scanning transmission electron microscopy (HAADF-STEM) and corresponding elemental mapping images (Figure 2i) show the homogenous distribution of Co, Ni, S, and P elements in P-$CoNi_2S_4$ YSSs.

XRD analysis (**Figure 3**a) indicates the similar diffraction patterns in $CoNi_2S_4$ YSSs and P-$CoNi_2S_4$ YSSs, which correspond well with the standard JCPDS card of No. 24-0334, manifesting that phosphorization would not destroy the crystal structure, which may be due to the similar atomic radius of S and P.[31,32] The average atomic ratio of P/S is determined to be about 0.9 from the EDX spectra (Figure 3b), giving about 47% substitution of the S sites. Further insights into the changes of surface chemical states after P doping could be acquired from the X-ray photoelectron spectroscopy (XPS) spectra. The peak-fitting analysis of Co 2p spectra (Figure 3c) suggests that two chemical states exist in both $CoNi_2S_4$ and P-$CoNi_2S_4$, corresponding to the spin-orbital characteristics of Co^{3+} (778.56 eV for $2p_{3/2}$ and 793.55 eV for $2p_{1/2}$) and Co^{2+} (781.50 eV for $2p_{3/2}$ and 798.01 eV for $2p_{1/2}$), accompanied with a pair of broad satellite peaks.[33,34] Similarly, the fitting peaks of Ni 2p spectra (Figure 3d) show two pairs of main peaks (853.27 eV for Ni^{2+} $2p_{3/2}$ and 870.43 eV for Ni^{2+} $2p_{1/2}$; 856.74 eV for Ni^{3+} $2p_{3/2}$ and 874.64 eV for Ni^{3+} $2p_{1/2}$) and two broad satellites.[34,35] Notably, the higher ratios of both Co^{2+}/Co^{3+} and Ni^{3+}/Ni^{2+} calculated by integrating the peak areas indicate much higher crystalline purity of $CoNi_2S_4$ in P-$CoNi_2S_4$, thereby being conducive to stronger redox reaction and enhancing the catalytic performance.[14,34,35] For the S 2p spectra in Figure 3e, both of them can be fitted with three distinct doublets of $2p_{3/2}$ and $2p_{1/2}$ with an area ratio of 2:1, including the first one (161.48 eV, 162.59 eV) that arises from a sulfide species, the second one (163.50 eV, 164.66 eV) indicative of sulfur in a thiolate-type environment, and the third one (168.81 eV, 169.97 eV) ascribed to surface oxidation.[31,32,36] Furthermore, the reduction in the area ratio of the fitting peaks belonging to oxides and sulfides in P-$CoNi_2S_4$ suggests phosphorization could suppress the oxidation of sulfides

in air.[24,32,34] The P 2p spectrum of P-$CoNi_2S_4$ (Figure 3f) only displays one doublet (133.52 eV, 134.39 eV) assigned to the P bonded with Co/Ni, no oxidized P species are observed.[31,37] This fully confirms the substitution characteristics of P, which will induce more electronic interactions for enriched Ni^{3+} content, thereby promoting electrocatalytic performance.

The electrocatalytic performance of P-$CoNi_2S_4$ YSSs for water splitting was first evaluated using a three-electrode configuration cell in alkaline media (1.0 M KOH, pH=14) at room temperature. **Figure 4**a shows the polarization curves of $CoNi_2S_4$ and P-$CoNi_2S_4$ towards HER, which are corrected for ohmic potential drop (iR) loss. The P-$CoNi_2S_4$ catalyst exhibits a smaller onset overpotential (20 mV, Figure S3, SI) than $CoNi_2S_4$, beyond which the cathodic current density rises rapidly under more negative potentials. Specifically, the P-$CoNi_2S_4$ catalyst requires a small overpotential of 135 mV to reach the current density of 10 mA cm^{-2}, which is a common criterion for evaluating the activity of water splitting.[38,39] Moreover, the P-$CoNi_2S_4$ catalyst displays a rapid rise in current density and constantly higher current density throughout the applied potential range, which is further evidenced by the analysis of Tafel slopes (Figure 4b). The reduction in Tafel slope from 81 mV dec^{-1} for $CoNi_2S_4$ to 65 mV dec^{-1} for P-$CoNi_2S_4$, together with the smaller overpotential of P-$CoNi_2S_4$ at the same current density, fully confirms the promotional effect of P substitution on the activity and kinetics of alkaline HER. This enhancement may be due to the electronic modulation effect of P on metal and/or S sites to facilitate the water dissociation, and in addition the P sites could also serve as the active sites for HER.[10,40-42] Moreover, the P-$CoNi_2S_4$ catalyst shows superior HER activity and kinetics when compared to some previously reported sulfide-based electrocatalysts (Table S1, SI). The 40-h chronopotentiometry test (Figure S4, SI) also shows the superior catalytic stability of P-$CoNi_2S_4$.

The iR-compensated cyclic voltammetry (CV) curves of these two samples (Figure S5, SI) both show the pre-oxidation process to generate catalytically active high-valence species.[22,43-45] To avoid

the effect of oxidation peak, we use the reverse sweep branch of the CV curve to evaluate the OER activity and kinetics. As shown in Figure 4c,d, the OER activity and kinetics of $CoNi_2S_4$ have been greatly improved after P substitution, suggesting positive effects of P on OER. To reach a current density of 10 and 100 mA cm^{-2}, the P-$CoNi_2S_4$ catalyst requires overpotentials of 282 and 327 mV, respectively, which are lower than that of $CoNi_2S_4$ (288 and 349 mV). The smaller Tafel slope of 40 mV dec^{-1} for P-$CoNi_2S_4$ than that of $CoNi_2S_4$ (53 mV dec^{-1}) shows the faster OER reaction kinetics after P substitution. Such superior activity and kinetics of P-$CoNi_2S_4$ compare favorably with that of many sulfide-based OER electrocatalysts (Table S2, SI). In addition, the 60-h chronopotentiometry test (Figure S6, SI) also shows the superior catalytic stability of P-$CoNi_2S_4$ towards OER.

CV curves at different scan rates (Figure S7, SI) are measured to evaluate the electrochemically active surface area (ECSA).[9,38] As shown in Figure 4e, the P-$CoNi_2S_4$ catalyst shows a much higher value (4.7 mF cm^{-2}) than $CoNi_2S_4$ (2.6 mF cm^{-2}), indicating more exposed active sites in the former. The increased ECSA may be attributed to the formation of additional active sites that originated from the incorporation of P into $CoNi_2S_4$ by adjusting the catalytic properties of adjacent metal sites in the $CoNi_2S_4$,[46,47] which can be seen from the difference in the CV curves (Figure S5, SI). In addition, the incorporated P sites may serve as new active sites for water dissociation.[40,41] Electrochemical impedance spectroscopy (EIS) measurements are also performed to evaluate the charge-transfer resistance (R_{ct}), which is associated with electrocatalytic kinetics.[9,48,49] The smaller diameter of the semicircle in the high frequency region for P-$CoNi_2S_4$ suggests faster charge transfer and electrocatalytic kinetics (Figure 4f; Figure S8, SI), which may be due to the increase in electron delocalization induced by lone-pair electrons in 3p orbitals and empty 3d orbitals of phosphorus.[50,51] Previously reported density functional theory calculation results also confirm that P-doped sulfides display a much lower band gap than undoped sulfides due to the generation of new electronic states in the conduction band by P doping.[46,52] This effect of P substitution on increasing ECSA and decreasing R_{ct} is expected from previous studies, in which heteroatom doping or substitution has been

reported to be a versatile strategy for modulating the electronic and/or surface structures of the host materials.[26,31]

In view of the distinguished electrocatalytic performance of the as-prepared P-$CoNi_2S_4$ catalyst towards both HER and OER, a two-electrode electrolyzer was fabricated with P-$CoNi_2S_4$ as both the cathodic and anodic catalysts and 1.0 M KOH solution as the medium. The polarization curve for water electrolysis (Figure 4g) indicates the superior overall water splitting performance of the P-$CoNi_2S_4$||P-$CoNi_2S_4$ cell, which requires a low cell voltage of 1.544 V to afford a current density of 10 mA cm^{-2} compared to 1.533 V for a Pt/C||RuO_2 cell using commercial catalysts. More importantly, the advantage of this P-$CoNi_2S_4$||P-$CoNi_2S_4$ cell is much more significant at higher current densities. One can see that this low cell voltage of 1.544 V for P-$CoNi_2S_4$ is comparable or superior to that of the most efficient bifunctional electrocatalysts reported (Table S3, SI), including some recently reported values, such as 1.46 V for Mo-doped Ni_3S_2/Ni_xP_y hollow nanorods,[53] 1.58 V for CoFeO@black phosphorus,[54] 1.59 V for Fe_2CoPS_3,[55] and 1.62 V for Fe-Ni_2P@P-doped carbon/Cu_xS arrays.[56] Besides, the chronopotentiometry curves recorded at 10 mA cm^{-2} (Figure 4h) show that the P-$CoNi_2S_4$ catalyst exhibits outstanding overall water splitting durability over 100 h, much better than that of the Pt/C||RuO_2 cell. These results suggest that the as-prepared P-$CoNi_2S_4$ sample is a promising catalyst to replace noble metal catalysts for efficient and long-lasting hydrogen production in the practical water electrolysis device.

Although the P-$CoNi_2S_4$ catalyst exhibits excellent performance in overall water splitting, the energy efficiency for hydrogen production still needs to be further improved from the industrial application perspective. As mentioned earlier, UOR is an amiable anodic reaction to efficiently reduce the energy input for hydrogen generation.[13-16] The UOR performance of P-$CoNi_2S_4$ is evaluated through a three-electrode configuration in 1.0 M KOH solution containing 0.5 M urea (the concentration screening is shown in Figure S9, SI). To illustrate the electrocatalytic mechanism of

UOR, CV curves of P-$CoNi_2S_4$ in 1.0 M KOH solution with and without urea are plotted in **Figure 5**a for comparison. In the bare KOH solution, a typical pre-oxidation process occurs before OER, while when urea is added, the current density in the positive sweep dramatically increases. The potential to reach current densities of 10 and 100 mA cm^{-2} is drastically reduced to 1.306 and 1.367 V in 1.0 M KOH containing 0.5 M urea. A small Tafel slope of 55 mV dec^{-1} (Figure S10, SI) also well supports the observed rapid increment in the current density, indicating the fast kinetics towards UOR. Such superior UOR performance endows the as-prepared P-$CoNi_2S_4$ as one of the state-of-the-art Ni-based electrocatalysts (Table S4, SI). Moreover, the negligible anodic current for OER compared with that for UOR demonstrates the superior selectivity of P-$CoNi_2S_4$ towards UOR at low potential (<1.5 V vs. RHE). The smaller reduction peak in the reverse sweep branch of CV curves also indicates that metal species are mostly involved directly in UOR rather than pre-oxidized to catalyze OER.[57] Both branches of the CV curves confirm the low onset potential for UOR, which is close to the onset potential of pre-oxidation, proving that the high-valence metal species promotes the catalysis of urea.[14,16,57] The UOR rate capability of P-$CoNi_2S_4$ is studied by tuning the scan rate from 2 to 100 mV s^{-1} (Figure 5b). The current density and square root of the scan rate maintain a good linear relationship at 1.40 V vs. RHE (inset in Figure 5b), which indicates that UOR is a surface controlled process with highly efficient charge and mass transfer.[16,58]

To verify the feasibility of UOR as an alternative anodic reaction, the HER activity of P-$CoNi_2S_4$ is also evaluated in a 1.0 M KOH solution containing 0.5 M urea. The almost overlapped LSV curves (Figure S11, SI) indicate the negligible influence of urea on the HER activity, showing the bifunctional activity of P-$CoNi_2S_4$ towards both HER and UOR. Subsequently, a two-electrode configuration in 1.0 M KOH solution containing 0.5 M urea is fabricated using P-$CoNi_2S_4$ as both the anode and cathode to perform urea-assisted electrochemical hydrogen production. As shown in Figure 5c, the cell voltage to achieve the current density of 10 mA cm^{-2} is 1.402 V, which is much lower than that required for water splitting (1.544 V), proving the assistance of urea oxidation can

lower the energy consumption of hydrogen production. The performance of P-$CoNi_2S_4$ in overall urea electrolysis is also superior to that of many other electrocatalysts (Table S5, SI). Furthermore, the chronopotentiometry curve recorded at 10 mA cm^{-2} (Figure 5d) shows good durability with only a 26 mV increment in the cell voltage after a continuous operation of 100 h. The excellent catalytic activity and long-term durability indicate that the synthesized P-$CoNi_2S_4$ YSSs might serve as a low-cost and high-efficiency bifunctional electrocatalyst for feasible urea-assisted electrochemical hydrogen production.

In summary, we have rationally designed and synthesized phosphorus-substituted bimetallic cobalt-nickel sulfide yolk-shell spheres (P-$CoNi_2S_4$ YSSs) via composition manipulation and nano-structure engineering. Thanks to the desired composition and structure, the obtained P-$CoNi_2S_4$ YSSs exhibit excellent electrocatalytic performance for HER and OER, giving rise to reduced cell voltage in overall water splitting. Moreover, the enriched Ni^{3+} content induced by P substitution endows the P-$CoNi_2S_4$ YSSs one of the state-of-the-art UOR catalysts with a low potential of 1.306 V vs. RHE at 10 mA cm^{-2}. When replacing OER with more amiable UOR, the urea-mediated electrolysis cell requires a very low potential of 1.402 V to reach 10 mA cm^{-2}, which is 142 mV less than that required for water splitting. This work provides a feasible and efficient strategy for the design and synthesis of high-performance electrocatalysts based on multifunctional nickel-based sulfides, which might open an avenue towards cost-effective and energy-saving electrochemical hydrogen production as well as promote the advancement of sulfides in related energy and environmental fields.

Acknowledgements

X.W.L. acknowledges the funding support from the Ministry of Education of Singapore through Academic Research Fund (AcRF) Tier-1 funding (RG116/18).

References

[1] J. A. Turner, *Science* **2004**, *305*, 972.

[2] O. J. Guerra, J. Eichman, J. Kurtz, B.-M. Hodge, *Joule* **2019**, *3*, 2425.

[3] Y. Li, X. Wei, L. Chen, J. Shi, *Angew. Chem. Int. Ed.* **2020**, DOI: 10.1002/anie.202009854.

[4] H. I. Karunadasa, C. J. Chang, J. R. Long, *Nature* **2010**, *464*, 1329.

[5] J. Wang, F. Xu, H. Jin, Y. Chen, Y. Wang, *Adv. Mater.* **2017**, *29*, 1605838.

[6] B. M. Hunter, H. B. Gray, A. M. Müller, *Chem. Rev.* **2016**, *116*, 14120.

[7] J. Song, C. Wei, Z. F. Huang, C. Liu, L. Zeng, X. Wang, Z. J. Xu, *Chem. Soc. Rev.* **2020**, *49*, 2196.

[8] Q. Shi, C. Zhu, D. Du, Y. Lin, *Chem. Soc. Rev.* **2019**, *48*, 3181.

[9] Z. P. Wu, X. F. Lu, S. Q. Zang, X. W. Lou, *Adv. Funct. Mater.* **2020**, *30*, 1910274.

[10] C. X. Zhao, J. N. Liu, J. Wang, D. Ren, B. Q. Li, Q. Zhang, *Chem. Soc. Rev.* **2021**, *50*, 7745.

[11] J. Zhu, L. Hu, P. Zhao, L. Y. S. Lee, K. Y. Wong, *Chem. Rev.* **2020**, *120*, 851.

[12] C. Hu, L. Zhang, J. Gong, *Energy Environ. Sci.* **2019**, *12*, 2620.

[13] B. Zhu, Z. Liang, R. Zou, *Small* **2020**, *16*, 1906133.

[14] L. Wang, Y. Zhu, Y. Wen, S. Li, C. Cui, F. Ni, Y. Liu, H. Lin, Y. Li, H. Peng, B. Zhang, *Angew. Chem. Int. Ed.* **2021**, *60*, 10577.

[15] X. Hu, J. Zhu, J. Li, Q. Wu, *ChemElectroChem* **2020**, *7*, 3211.

[16] B. K. Boggs, R. L. King, G. G. Botte, *Chem. Commun.* **2009**, 4859.

[17] S. De, J. Zhang, R. Luque, N. Yan, *Energy Environ. Sci.* **2016**, *9*, 3314.

[18] V. Vij, S. Sultan, A. M. Harzandi, A. Meena, J. N. Tiwari, W.-G. Lee, T. Yoon, K. S. Kim, *ACS Catal.* **2017**, *7*, 7196.

[19] D. A. Daramola, D. Singh, G. G. Botte, *J. Phys. Chem. A* **2010**, *114*, 11513.

[20] J. Yin, J. Jin, H. Zhang, M. Lu, Y. Peng, B. Huang, P. Xi, C. H. Yan, *Angew. Chem. Int. Ed.* **2019**, *58*, 18676.

[21] L. Trotochaud, S. L. Young, J. K. Ranney, S. W. Boettcher, *J. Am. Chem. Soc.* **2014**, *136*, 6744.

[22] J. M. P. Martirez, E. A. Carter, *ACS Catal.* **2020**, *10*, 2720.

[23] J. Hu, C. Zhang, X. Meng, H. Lin, C. Hu, X. Long, S. Yang, *J. Mater. Chem. A* **2017**, *5*, 5995.

[24] H. J. Song, H. Yoon, B. Ju, G.-H. Lee, D.-W. Kim, *Adv. Energy Mater.* **2018**, *8*, 1802319.

[25] H. Qin, B. Zhang, Y. Pan, X. Wang, L. Diao, J. Chen, J. Wu, E. Liu, J. Sha, L. Ma, *J. Catal.* **2020**, *381*, 493.

[26] S. Huang, Z. Jin, P. Ning, C. Gao, Y. Wu, X. Liu, P. Xin, Z. Chen, Y. Jiang, Z. Hu, Z. Chen, *Chem. Eng. J.* **2020**, *420*, 127630.

[27] L. Yu, H. B. Hu, H. B. Wu, X. W. Lou, *Adv. Mater.* **2017**, *29*, 1604563.

[28] X. F. Lu, S. L. Zhang, E. Shangguan, P. Zhang, S. Gao, X. W. Lou, *Adv. Sci.* **2020**, *7*, 2001178.

[29] H. Chen, K. Shen, Y. Tan, Y. Li, *ACS Nano* **2019**, *13*, 7800.

[30] L. Shen, L. Yu, H. B. Wu, X. Y. Yu, X. Zhang, X. W. Lou, *Nat. Commun.* **2015**, *6*, 6694.

[31] W. Liu, E. Hu, H. Jiang, Y. Xiang, Z. Weng, M. Li, Q. Fan, X. Yu, E. I. Altman, H. Wang, *Nat. Commun.* **2016**, *7*, 10771.

[32] Z. Dai, H. Geng, J. Wang, Y. Luo, B. Li, Y. Zong, J. Yang, Y. Guo, Y. Zheng, X. Wang, Q. Yan, *ACS Nano* **2017**, *11*, 11031.

[33] A. Sivanantham, P. Ganesan, S. Shanmugam, *Adv. Funct. Mater.* **2016**, *26*, 4661.

[34] H. Gu, W. Fan, T. Liu, *Nanoscale Horiz.* **2017**, *2*, 277.

[35] Y. Liu, Y. Wen, Y. Zhang, X. Wu, H. Li, H. Chen, J. Huang, G. Liu, S. Peng, *Sci. China Mater.* **2020**, *63*, 1216.

[36] J. Kibsgaard, T. F. Jaramillo, *Angew. Chem. Int. Ed.* **2014**, *53*, 14433.

[37] Y. Tong, P. Chen, L. Chen, X. Cui, *ChemSusChem* **2021**, *14*, 2576.

[38] C. C. McCrory, S. Jung, I. M. Ferrer, S. M. Chatman, J. C. Peters, T. F. Jaramillo, *J. Am. Chem. Soc.* **2015**, *137*, 4347.

[39] X. F. Lu, L. Yu, X. W. Lou, *Sci. Adv.* **2019**, *5*, eaav6009.

[40] C. Hu, Q. Ma, S.-F. Hung, Z.-N. Chen, D. Ou, B. Ren, H. M. Chen, G. Fu, N. Zheng, *Chem* **2017**, *3*, 122.

[41] Y. Li, Z. Mao, Q. Wang, D. Li, R. Wang, B. He, Y. Gong, H. Wang, *Chem. Eng. J.* **2020**, *390*, 124556.

[42] X. Li, X. H. Wang, Y. Nie, B. X. Tao, Y. X. Yang, W. H. Guo, J. Zhang, Z. Cai, Y. Ling, W. Liu, H. Q. Luo, N. B. Li, *J. Catal.* **2020**, *382*, 228.

[43] H. Wang, H. W. Lee, Y. Deng, Z. Lu, P. C. Hsu, Y. Liu, D. Lin, Y. Cui, *Nat. Commun.* **2015**, *6*, 7261.

[44] S. F. Hung, Y. T. Chan, C. C. Chang, M. K. Tsai, Y. F. Liao, N. Hiraoka, C. S. Hsu, H. M. Chen, *J. Am. Chem. Soc.* **2018**, *140*, 17263.

[45] Y. Huang, S. L. Zhang, X. F. Lu, Z.-P. Wu, D. Luan, X. W. Lou, *Angew. Chem. Int. Ed.* **2021**, *60*, 11841.

[46] B. Qiu, L. Cai, Y. Wang, X. Guo, S. Ma, Y. Zhu, Y. H. Tsang, Z. Zheng, R. Zheng, Y. Chai, *Small* **2019**, *15*, 1904507.

[47] D. Lim, C. Lim, M. Hwang, M. Kim, S. E. Shim, S.-H. Baeck, *J. Power Sources* **2021**, *490*, 229552.

[48] R. Miao, B. Dutta, S. Sahoo, J. He, W. Zhong, S. A. Cetegen, T. Jiang, S. P. Alpay, S. L. Suib, *J. Am. Chem. Soc.* **2017**, *139*, 13604.

[49] S. L. Zhang, B. Y. Guan, X. F. Lu, S. Xi, Y. Du, X. W. Lou, *Adv. Mater.* **2020**, *32*, 2002235.

[50] H. Yan, C. Tian, L. Wang, A. Wu, M. Meng, L. Zhao, H. Fu, *Angew. Chem. Int. Ed.* **2015**, *54*, 6325.

[51] F. Zhang, Y. Ge, H. Chu, P. Dong, R. Baines, Y. Pei, M. Ye, J. Shen, *ACS Appl. Mater. Interfaces* **2018**, *10*, 7087.

[52] C. Liu, D. Jia, Q. Hao, X. Zheng, Y. Li, C. Tang, H. Liu, J. Zhang, X. Zheng, *ACS Appl. Mater. Interfaces* **2019**, *11*, 27667.

[53] X. Luo, P. Ji, P. Wang, R. Cheng, D. Chen, C. Lin, J. Zhang, J. He, Z. Shi, N. Li, S. Xiao, S. Mu, *Adv. Energy Mater.* **2020**, *10*, 1903891.

[54] X. Li, L. Xiao, L. Zhou, Q. Xu, J. Weng, J. Xu, B. Liu, *Angew. Chem. Int. Ed.* **2020**, *59*, 21106.

[55] J. Tong, C. Li, L. Bo, X. Guan, Y. Wang, D. Kong, H. Wang, W. Shi, Y. Zhang, *Int. J. Hydrogen Energy* **2021**, *46*, 3354.

[56] D. T. Tran, H. T. Le, V. H. Hoa, N. H. Kim, J. H. Lee, *Nano Energy* **2021**, *84*, 105861.

[57] D. Khalafallah, C. Ouyang, M. Zhi, Z. Hong, *ChemCatChem* **2020**, *12*, 2283.

[58] M. He, S. Hu, C. Feng, H. Wu, H. Liu, H. Mei, *Int. J. Hydrogen Energy* **2020**, *45*, 23.

Figures and captions

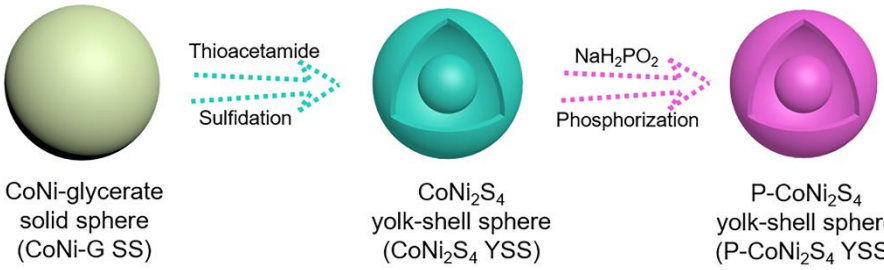

Figure 1. Schematic illustration of the preparation of P-$CoNi_2S_4$ YSSs.

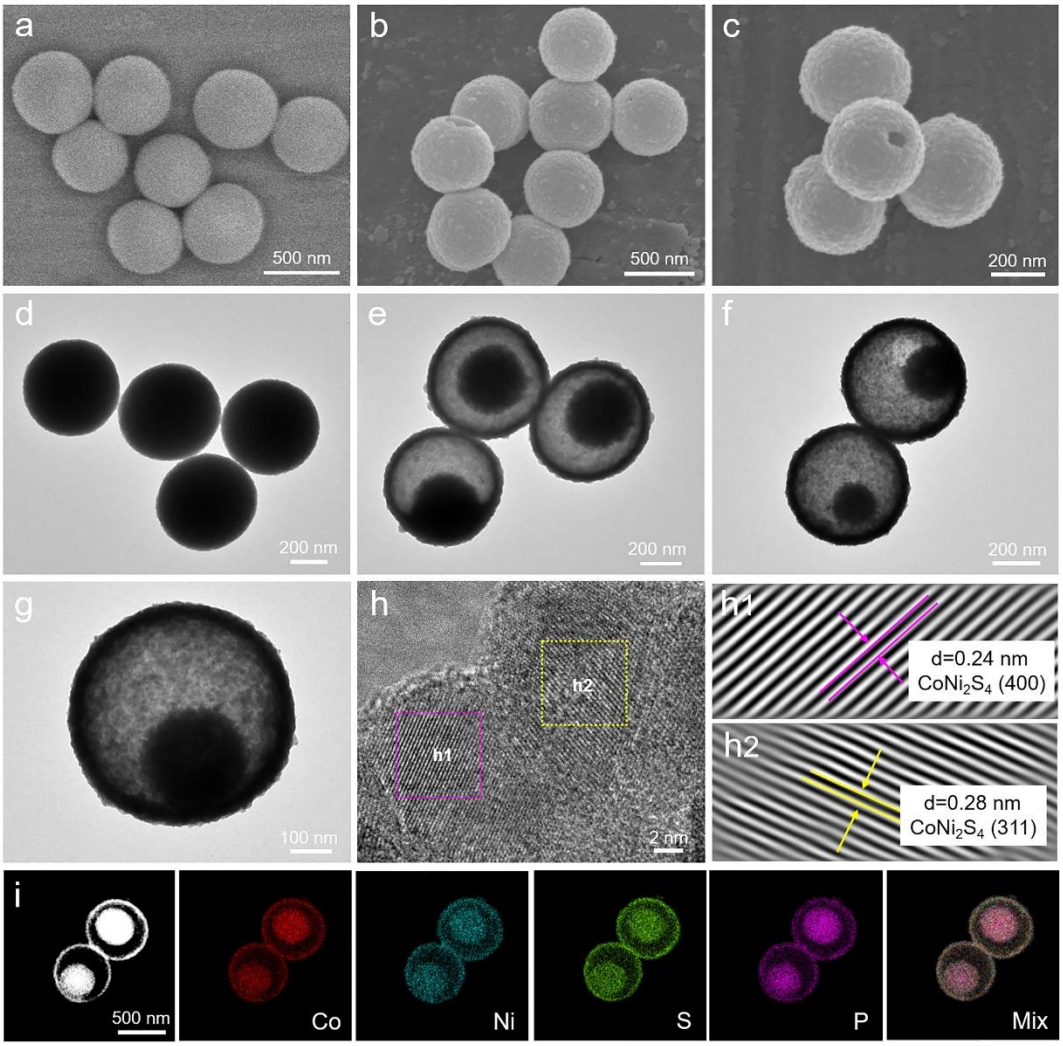

Figure 2. (a-c) FESEM and (d-g) TEM images of CoNi-G SSs (a,d), $CoNi_2S_4$ YSSs (b,e), and P-$CoNi_2S_4$ YSSs (c,f,g). (h) HRTEM image, (h1,h2) the inverse fast Fourier transformation (IFFT) images, and (i) elemental mapping images of P-$CoNi_2S_4$ YSSs.

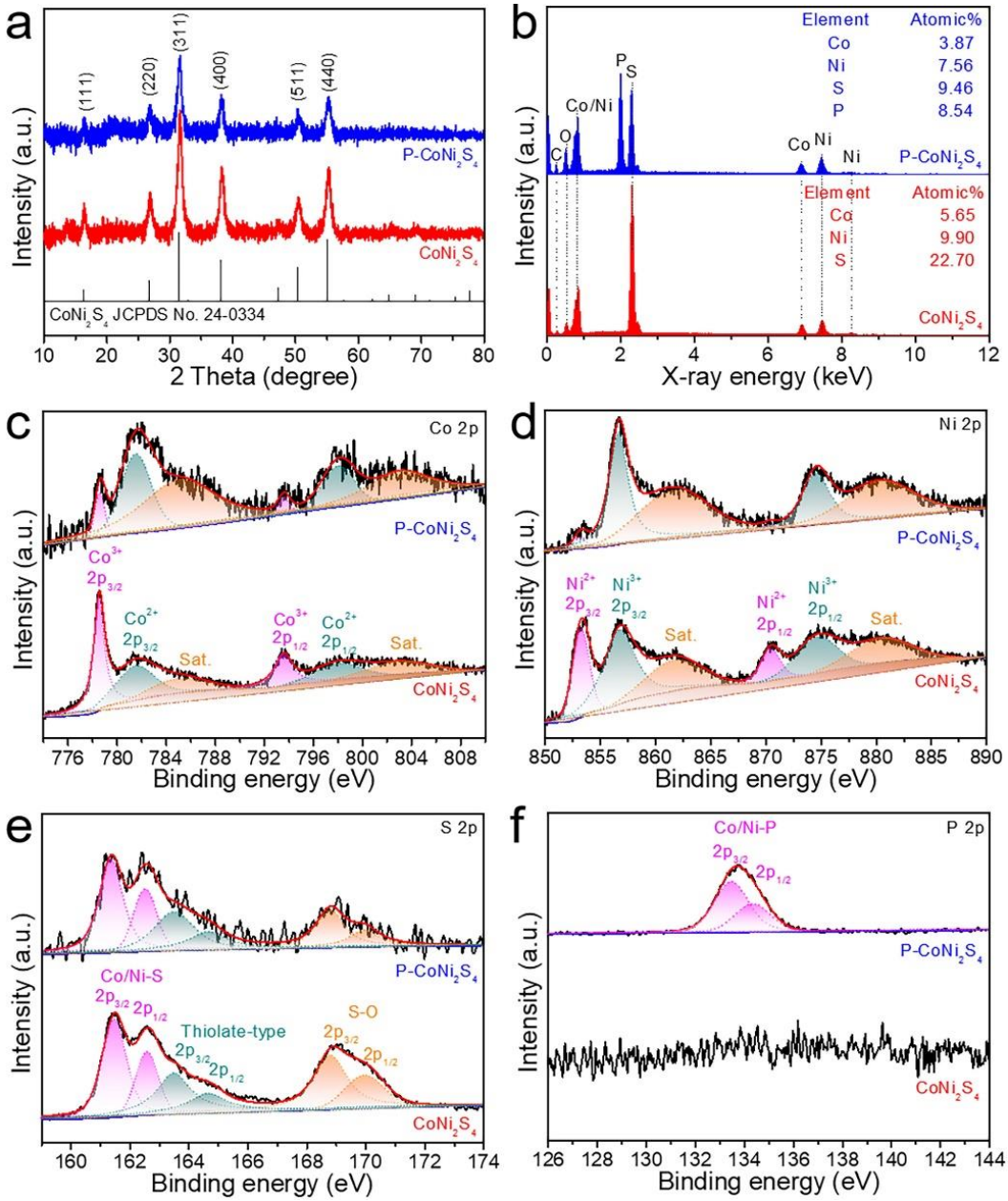

Figure 3. (a) XRD patterns, (b) EDX spectra, and (c-f) high-resolution XPS spectra of Co 2p (c), Ni 2p (d), S 2p (e), and P 2p (f) of $CoNi_2S_4$ YSSs and P-$CoNi_2S_4$ YSSs.

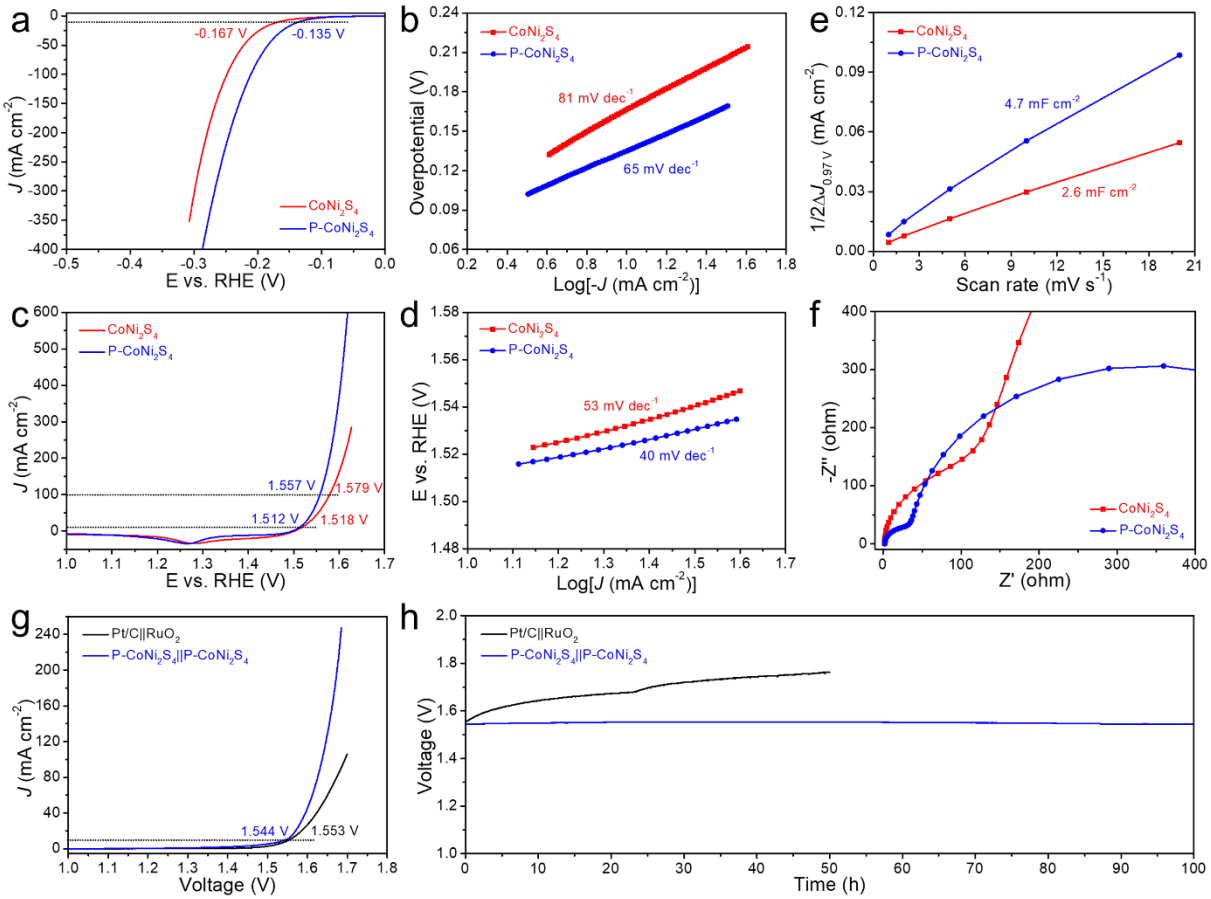

Figure 4. (a) LSV curves and (b) corresponding Tafel slopes of $CoNi_2S_4$ YSSs and P-$CoNi_2S_4$ YSSs towards HER. (c) CV curves in the reverse sweep and (d) corresponding Tafel slopes of $CoNi_2S_4$ YSSs and P-$CoNi_2S_4$ YSSs towards OER. (e) Half of the capacitive current density difference at 0.97 V vs. RHE as a function of the scan rate and (f) EIS spectra of $CoNi_2S_4$ YSSs sand P-$CoNi_2S_4$ YSSs. (g) LSV curves and (h) chronopotentiometry curves at 10 mA cm^{-2} of P-$CoNi_2S_4$||P-$CoNi_2S_4$ and Pt/C||RuO_2 couples towards overall water splitting.

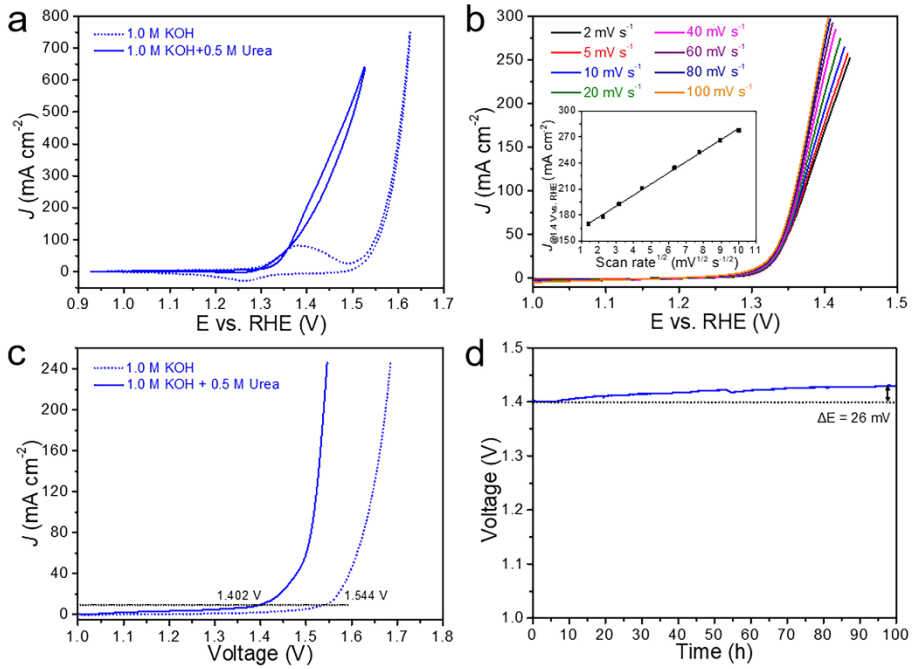

Figure 5. (a) CV curves of P-$CoNi_2S_4$ YSSs towards OER and UOR. (b) LSV curves of P-$CoNi_2S_4$ YSSs for UOR at scan rates from 2 to 100 mV s^{-1} (Inset is the relationship between the current density at 1.4 V vs. RHE and square root of the scan rate). (c) Polarization curves of P-$CoNi_2S_4$ YSSs towards water splitting and urea electrolysis. (d) Chronopotentiometry curve at 10 mA cm^{-2} of bifunctional P-$CoNi_2S_4$ YSSs towards urea electrolysis.

for Table of Content Entry

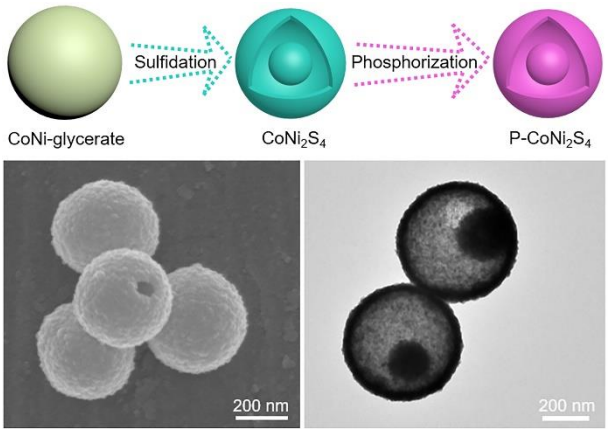

Phosphorus substituted $CoNi_2S_4$ yolk-shell spheres (P-$CoNi_2S_4$ YSSs) have been rationally designed and synthesized by a facile hydrothermal sulfidation and subsequent gas-phase phosphorization strategy. The desired hollow structure and multi-element composition with abundant Ni^{3+} active sites endow P-$CoNi_2S_4$ YSSs with high electrocatalytic activity and robust stability towards electrochemical hydrogen production via water splitting and urea electrolysis.